

An experiment to distinguish persistent infrasounds from two fumaroles at Kirishima Iwo-Yama

Kazuya Yamakawa (✉ sanga6681@gmail.com)

Yamanashi Prefecture: Yamanashi-ken <https://orcid.org/0000-0003-0113-4046>

Mie Ichihara

University of Tokyo: Tokyo Daigaku

Dan Muramatsu

University of Tokyo: Tokyo Daigaku

Takeshi Matsushima

Kyushu University: Kyushu Daigaku

Hidetoshi Takahashi

Keio University: Keio Gijuku Daigaku

Ruka Wada

Keio University: Keio Gijuku Daigaku

Isao Shimoyama

Toyama Prefectural University Libraries: Toyama Kenritsu Daigaku Fuzoku Toshokan

Research Article

Keywords: Infrasound, Volcano, Fumarole, Array observation

Posted Date: May 17th, 2022

DOI: <https://doi.org/10.21203/rs.3.rs-1632226/v1>

License:   This work is licensed under a Creative Commons Attribution 4.0 International License.

[Read Full License](#)

Version of Record: A version of this preprint was published at Earth, Planets and Space on February 21st, 2023. See the published version at <https://doi.org/10.1186/s40623-023-01777-9>.

Abstract

In the infrasonic observation of fumarolic area, the challenge is to distinguish among the multiple fumarolic sources and noise. The array technique effectively estimates the source locations and identifies the target signal from others and noise. We conducted the experiment at Kirishima Iwo-yama, Japan, where there are two fumarolic craters separated by about 450 m. A three-element array with an aperture of 20 m was installed between two targeting fumaroles. In addition, a single microphone was installed near one of the fumaroles. The array with the waveform correlation analysis estimated the most prominent source but failed to estimate the other weak source. The joint analysis of the array and the single microphone effectively resolved the two sources. The method developed by this experiment would be beneficial for monitoring volcanoes that hold hydrothermally active multiple vents.

1. Introduction

Distinguishing multiple sources is a challenge in the infrasonic monitoring of volcanoes. Many volcanoes have multiple vents. In Stromboli, several vents are active simultaneously (e.g., Chouet et al. 1997; Ripepe et al. 2002; Salvatore et al. 2018; Yamakawa et al. 2022). Multiple new vents emanating infrasound are formed by flank eruptions like the eruptions of Etna, Italy (the 2006 eruption, Marchetti et al. 2009; the 2007 eruption, Cannata et al. 2009) and the 2007 eruption of Kilauea, Hawaii (Fee et al. 2011) and by phreatic eruptions like the 2018 eruption of Kirishima Iwo-Yama, Japan (Muramatsu et al. 2021). In history, Sakurajima is known to have erupted at two places simultaneously (Iguchi 2013). In many cases, infrasound analysts avoid the multiple sources problem by choosing the time windows or assuming that the most significant single source mainly produces the observed waveform (e.g., Ripepe and Marchetti 2002; Yokoo et al. 2014; Yamakawa et al. 2022). These methods are effective in case a transient large-amplitude signal, such as an explosion wave, is observed or a single crater's activity is more significant than the others. However, the multiple sources matter when no signal is dominant because of low amplitudes or comparable multiple active sources.

A fumarole is a vent that emanates steam and other volatiles, like carbon dioxide and sulfur dioxide, in an active volcanic environment (McKee et al. 2017). It brings us information about volcanic activity (Wallace 2005; Fischer 2008). Fumaroles are active even when the volcano is not active enough to erupt. Thus, fumaroles are also useful as observation targets in field experiments. Some studies focused on the acoustic noise emanated from a fumarole (Woulff and McGetchin 1976; McKee et al. 2017). McKee et al. (2017) investigated fumarolic noise at Aso Volcano (Japan), where the gas jetting fumarole in Naka-dake crater was active. They found low-amplitude sustained broadband (0.5 to 25 Hz) infrasonic signals and compared their power spectra with the laboratory jet noise spectra (Tam et al. 2008) to estimate the jet velocity. Eventually, they converted the jet velocity to the total volatile flux. Their work suggested a new monitoring method of the fumarole.

An active hydrothermal field often holds multiple fumaroles within several hundred meters (Aiuppa et al. 2005; Tajima et al. 2020). Since the fumarolic noise is weak, it is often obscured by wind noise. The very-

small-aperture (VSA) array having a few tens of meters aperture (Yamakawa et al. 2018; Yamakawa et al. 2022) should contribute to this problem. We conducted an experiment using a VSA array at Kirishima Iwo-Yama and tried to resolve the multiple fumarolic sources. This paper presents the results and discusses the performance and limitations of a VSA array observation for resolving multiple sources.

2. Kirishima Iwo-yama

The experiment was conducted on 19–20 October 2020 at Kirishima Iwo-Yama (hereafter noted as Iwo-Yama), Kyushu, Japan (Fig. 1), where several active fumaroles existed. Tajima et al. (2020) documented the activity of Kirishima Iwo-Yama. The fumarolic activities have been varying with the change of the thermal anomaly area since December 2015. The apparent activity of jet fumaroles around the Iwo-Yama south crater (hereafter noted as ISC) started in 2017. After the phreatic eruption of Iwo-Yama on 19 April 2018, the Iwo-Yama west crater (hereafter noted as IWC) started to be active. The infrasonic activities of ISC and IWC during the phreatic eruption in April 2018 were reported by Muramatsu et al. (2021). They identified the simultaneous two signals: the major one from ISC and the moderate one from IWC, analyzing data from two microphones (Fig. 1 a). During the experiment of this paper (19–20 October 2020), the activities of the two craters were minor but still ongoing. The main purpose of this paper is to resolve the infrasonic signals from these two craters, particularly the Y2a and Y3 vents in ISC and the W4 vent in IWC (Tajima et al. 2020; Muramatsu et al. 2021). Hereafter, I refer to the Y2a and Y3 vents as the ISC fumarole and the W4 vent as the IWC fumarole.

3. Observation

A three-element VSA array with an aperture of 15 m was installed between the ISC and IWC fumaroles (Fig. 2). The distances from the array to the ISC and IWC fumaroles were 150 m and 300 m, respectively. The array was operated from 17:30 on 19 October 2020 to 12:30 on the next day. Referring to the nearest meteorological station, the temperature at Kirishima Iwo-Yama in the operation time is inferred to be from 2 to 18 °C.

We installed two types of newly developed microphones in the array to examine their performance. The one type, referred to as an ACO microphone, was a condenser microphone produced by ACO Co., which had been confirmed to have a sufficiently high performance for the VSA array (Yamakawa et al. 2022). The other, referred to as a MEMS microphone, was the microelectromechanical systems (MEMS) piezoresistive cantilever-type barometric pressure sensor (Takahashi et al. 2012; Minh-Dung et al. 2013) and had a high sensitivity and a power consumption as low as 1 mA (Wada and Takahashi 2020; Ikeda et al. 2022). The microphones were confirmed to record identical waveforms above 1 Hz in the laboratory experiment before the field experiment (Supporting Information S1).

At each array element, we put an ACO microphone and a MEMS microphone together in a small box to protect them from rain. Two three-channel 24-bit data loggers (LS8800, HAKUSAN Co.) individually recorded the data from the three ACO microphones and the three MEMS microphones at 200 Hz. The

microphones in the same array element recorded almost identical waveforms above 1 Hz (Fig. 2a1-a3, Supporting Information S2), where both ACO and MEMS microphones have flat responses (Supporting Information S1). As expected from the waveforms' similarity, the array analysis gave the same results with either ACO microphones or MEMS microphones, confirming the utility of both types of microphones in the VSA array. In this paper, we present the results with the three ACO microphones, which we refer to as A1, A2, and A3 microphones (Fig. 2).

In addition to the array, a single microphone (SI102, HAKUSAN) was installed near the IWC crater. Hereafter, we refer to it as the SI microphone. The distances from the SI microphone to the IWC and ISC fumaroles were ~ 15 m and ~ 450 m, respectively. The SI microphone was put in a box with a data logger (HKS-9700, KGC Co.), and the data were recorded at 1,000 Hz in 24 bit from 11:30 to 12:30 on 20 October 2020, when the temperature at Kirishima Iwo-Yama is inferred to be ~ 18 °C.

4. Analysis

Since the fumarole continuously emanated infrasound, the waveforms had no apparent onset. We mainly applied the grid search method for the lag time fitting with the cross-correlation maximization (Johnson and Palma 2015; Yamakawa et al. 2018). The length of the time window was 1 min. Sixty successive time windows overlapping by 59 sec were stacked. Namely, the 2-min-long data were used to obtain the cross-correlation. The mainly used frequency bands were 5–90 Hz.

The SI microphone was expected to record a significant signal from the IWC fumarole. Therefore, the cross-correlations between the SI and array microphones were also analyzed. Hereafter, we refer to the cross-correlations among the array elements as the “array CC” and the cross-correlations between the SI microphone and the array elements as the “SI-array CC.” Because we found the SI-array CC revealed the arrival time lags of signals from the two sources, we applied the lag time fitting method to the SI-array CC.

5. Results

Figure 2 shows the waveforms, spectrograms, and correlation coefficients of some selected microphones. Those of the other microphones are included in Supporting Information S3. The spectral structures of A1–A3 are similar (Fig. S3.1), though the waveforms of the individual array elements are sometimes different (Fig. 2a). The power below 5 Hz is significantly time-dependent (Fig. 2b). When the low-frequency power is large, the array CCs become poor (Fig. S3.2). We infer that the temporally varying low-frequency components are wind noise. When the wind speed is v , wind noise with a frequency f loses correlation beyond the distance of $v/f/3$ (Shields 2005). At a distance of 10 m, wind noise above 0.3 Hz should have little correlation under normal wind speeds. On the other hand, the higher components above 5 Hz are stable (Fig. 2c) and coherent among the array elements (Fig. 2e), indicating the existence of a steady infrasound signal. The SI microphone data exhibit waveforms and spectral structures different from the array microphones even above 5 Hz (Fig. 2a3 and 2d). We infer that the SI microphone might

have recorded signals from different sources. Here, we focus mainly on the steady signal above 5 Hz during the operation of all microphones (from 11:30 to 12:30 on 20 October). As mentioned in Section 4, we show the results using the waveforms band-pass filtered in 5–90 Hz. One of the reason is that the array CCs are almost the same among the different frequency bands (Supporting Information S3). The other reason is not to divide the SI-array CCs, which have a pretty small peak, in the frequency domain.

The array CC points to the ISC direction, while there seemed to be no apparent correlation corresponding to the IWC fumarole (Fig. 3a). We also tested with the MUSIC algorithm and the CLEAN beamforming (Supporting Information S4) but failed to identify the IWC fumarole's source.

The SI-array CC shows a prominent peak in the positive lag time and unclear small peaks in the negative lag time (Fig. 3b). By stacking the CCs for longer than 30 min, the small peaks become a single peak in each of the SI-array CCs (Fig. 3b1, Supporting Information S5). The lag times of these minor peaks pointed to the direction of IWC fumarole (Fig. 3c1), while the prominent peak (Fig. 3b2) corresponds to the direction of the ISC fumarole (Fig. 3c2). Ambient noise can also form peaks in the cross-correlation function between two stations, representing Green's function between the station pair (Shapiro and Campillo 2004; Ortiz et al. 2021). However, it is more probable that the observed correlation peaks are made of the fumarolic signals than ambient noise (discussed in Section 6.2). The result indicates that the SI-array CC analysis successfully identified the contribution of IWC fumarole with a time resolution of ~ 30 min.

Even if there are only two microphones (SI and one of the array elements, e.g., A1), the lag time of each peak of the single SI-array CC can constrain the source hyperbola. Both fumarolic areas are around the hyperbolas with the acoustic velocities of 340–345 m/s, which corresponding to the temperature of 14–23 °C (blue lines in Fig. 3d). Combining the hyperbola and the back-azimuth obtained by all the SI-array CCs (Fig. 3c) well constrained the source area (Fig. 3d).

Based on Parseval's theorem, the power spectrum can be derived from the correlation function. Since the SI-array CC resolved the contribution of each source, the Fourier transform of the SI-array CC in a limited lag-time range around each peak should show the PSD of the corresponding source signal. Thus, we obtained the PSDs of the ISC fumarole signal (Fig. 3e1) and the IWC fumarole signal (Fig. 3e2).

6. Discussion

6.1. The power ratio of the two sources

Some array-analysis methods, such as MUSIC and CLEAN beamforming, are expected to resolve multiple sources. However, even in the analyses of the SI-array correlation, the array analyses identified only the ISC fumarole signals. Namely, the analyses failed to distinguish the ISC and IWC fumaroles simultaneously. One of the reasons for this failure should be the significantly larger power of the ISC fumarole signal than the IWC's. To know the individual source contributions to the observed waveforms, we estimate their powers, assuming simple monopole sources (Woulff and McGetchin 1976).

The monopole source amplitudes can be calculated from the peak values of the cross-correlation functions and the source-receiver distances. We model the waveforms $F^a(t)$ at the array and $F^b(t)$ at the SI microphone as follows:

$$F^a(t) = \frac{S_1(t - \tau_1^a)}{|y_1 - x^a|} + \frac{S_2(t - \tau_2^a)}{|y_2 - x^a|} + N^a(t), \quad (1)$$

$$F^b(t) = \frac{S_1(t - \tau_1^b)}{|y_1 - x^b|} + \frac{S_2(t - \tau_2^b)}{|y_2 - x^b|} + N^b(t), \quad (2)$$

where x^n and $N^n(t)$ indicate the location and noise at the station n (a or b), $S_m(t)$ and y_m indicate the source time function and location of the source m (1 or 2), and τ_m^n indicates the travel time from the source m to the station n . For the convenience, we define $\Delta\tau_m = \tau_m^b - \tau_m^a$ and $\Delta\tau^n = \tau_2^n - \tau_1^n$. We assume that the correlations between the two sources, source and noise, and noise at the two stations are negligible, namely, $E[S_1(t)S_2(t)] = E[S_m(t)N^n(t)] = E[N^a(t)N^b(t)] = 0$, where $E[\bullet]$ is the ensemble average. In addition, since $\Delta\tau_1$ and $\Delta\tau_2$ are significantly different (the locations of the colored dotted lines and colored dashed lines in Fig. 4b, respectively), the correlation between $S_m(t - \Delta\tau_1)$ and $S_m(t - \Delta\tau_2)$ is assumed to be negligible compared to the power of sources, namely, $E[S_1(t)S_1(t)] \gg E[S_2(t - \Delta\tau_1)S_2(t - \Delta\tau_2)]$ and $E[S_2(t)S_2(t)] \gg E[S_1(t - \Delta\tau_1)S_1(t - \Delta\tau_2)]$. Considering the general relation that $E[f_1(t)f_2(t+T)] = E[f_1(t-T)f_2(t)]$ for arbitrary functions f_1 and f_2 , we get the relation that $E[S_m(t - \Delta\tau_1)S_m(t - \Delta\tau_2)] = E[S_m(t - \Delta\tau^a)S_m(t - \Delta\tau^b)]$. Then, we can calculate the power of the sources PS_1 and PS_2 as follows:

$$PS_m = E[S_m(t)S_m(t)] \simeq |y_m - x^a||y_m - x^b| E[F^a(t + \tau_m^a)F^b(t + \tau_m^b)], \quad (3)$$

where $E[F^a(t + \tau_m^a)F^b(t + \tau_m^b)]$ could be evaluated by the peak value of the cross-correlation (Fig. 4b). Once PS_1 and PS_2 are obtained, we can calculate the noise power at the n -th station PN^n as follows:

$$PN^n = E[F^n(t)F^n(t)] - \frac{PS_1}{|y_1 - x^n|^2} - \frac{PS_2}{|y_2 - x^n|^2}. \quad (4)$$

Since the propagation effect or the directionality of the source might lose the correlation values, this method using the cross-correlation peak values might underestimate the source power. Nevertheless, it should give us approximate powers of the sources.

The results are shown in Table 1. The source amplitude of the ISC fumarole is estimated to be larger than the IWC fumarole by one or two orders of magnitude. Although the SI microphone was near the IWC fumarole (~ 15 m distance), the ISC fumarole's power was comparable to the IWC fumarole. It

emphasizes that it is crucial to identify the multiple sources, even when we put a microphone very close to a target source.

6.2. Correlation signal

The ambient noise around two stations is known to generate peaks in the stacked correlation function, which represents Green's functions between the stations (Shapiro and Campillo 2004; Ortiz et al. 2021). In other words, the stacked correlation function of a station pair can hold two minor but significant peaks without any particular signals. Since the IWC peak in SI-array CC is pretty small, it is not easy to distinguish whether it corresponds to Green's function or the IWC fumarole signal. In the former case, there should be another minor peak around + 0.8 sec in the SI-array CC because two correlation signals should emerge symmetrically with respect to the zero lag time. However, the correlation peak of the ISC fumarole signal may mask such a peak (Fig. 3b2). Besides, since the IWC fumarole and the SI microphone are close, it is not easy to identify which is the source by the array analysis (Fig. 3d1).

To solve this problem, we conducted some synthetic tests. The locations of stations are simplified that all the stations and fumaroles are on a single plane (Fig. 4a). The waveform, $F^n(t)$, recorded at n -th microphone at x^n consists of four types of waves:

$$F^n(t) = A_1 \frac{s_1(t - \tau_1^n)}{|y_1 - x^n|} + A_2 \frac{s_2(t - \tau_2^n)}{|y_2 - x^n|} + A_{\text{noise}}^n s_{\text{noise}}^n(t) + \sum_k A_k \frac{s_k(t - \tau_k^n)}{|y_k - x^n|}, \quad (5)$$

where s_1 and s_2 are the normalized synthetic waveforms from the ISC and IWC fumaroles, s_{noise}^n is the uncorrelated noise at n -th microphone, and s_k is the normalized noise from the k -th of the numerous background acoustic sources. Their amplitudes are denoted by A_1 , A_2 , A_{noise}^n , and A_k , respectively. The source-to-station propagation times of the acoustic waves are τ_1^n , τ_2^n , and τ_k^n , and the source locations are y_1 , y_2 , and y_k , respectively. We put 7,000–8,000 ambient sources within 2 km from the stations but excluded 400 m from the mid-point to avoid ambient sources having a larger power than the fumarolic signals (Fig. 4a). I mainly tested the ambient noise sources in the same plane as the microphones because they made more distinct correlation signals than those out of the plane. Gaussian noise in 5–80 Hz is used as the synthetic waveforms. The correlation coefficients are calculated in 1 min time windows with 60 min stacking.

Several conditions are tested (Table 2) and compared for both SI-array CC and array CC between the observation (Figs. 4b and 4c) and synthetic tests (Fig. 4b1–b5 and 4c1–c5). The comparison results are summarized in Table 2. As was expected, the ambient noise generated the correlation signals without particular sources (Test 1: Fig. 4b1 and 4c1). The peak values of the correlation signals in the SI-array CC were as small as the minor peak of the observation (Fig. 4c and 4c). In the test using a synthetic ISC signal with an adequate amplitude and ambient noise, the peak values of the array CC in the synthetic test were smaller than the observation, though the peak values of the SI-array CC were similar to the observation (Test 2: Fig. 4b2 and 4c2). A larger synthetic ISC signal could reproduce the observed peak values of the array CC. However, it also made a too large ISC peak value of the SI-array CC (Test 3:

Fig. 4b3 and 4c3) while weakening the peak of the correlation signal at -0.8 s. Adding uncorrelated noise on the SI microphone could suppress the SI-array CC but erased the correlation signal at -0.8 s (Test 4: Fig. 4b4 and 4c4). The existence of the IWC fumarole signal was necessary to explain all the peak values of the correlation coefficients (Test 5: Fig. 4b5 and 4c5, Table 2), at least in these synthetic tests. From above, we concluded that the IWC fumarole's signal formed the minor peak in the SI-array CC.

6.3. Power spectrum

At the array, the contribution of the ISC fumarole is significant (Table 1). Thus, the power spectrum of the array elements (the green line in Fig. 3e) is expected to represent the infrasound signal character from the ISC fumarole. The distinct feature is the persistent power in ~ 10 Hz and ~ 35 Hz. Although both correlation functions corresponding to the IWC and ISC signals have significant power in ~ 35 Hz (the red line in Fig. 3e1 and the blue line in Fig. 3e2, respectively), the numerical tests using synthetic waveforms confirmed that the power in ~ 35 Hz should be from the ISC signal (Supporting Information S6).

The mechanism generating the power in ~ 10 Hz or ~ 35 Hz would be important for the investigation of the fumarole. In volcanoes, the harmonic monochromatic sources are often observed and modeled (e.g., Fee et al. 2010; Ripepe et al. 2010; Goto et al. 2011; Yokoo et al. 2019). The topographical resonance under the ground is often discussed, such as the Helmholtz resonance (Fee et al. 2010; Goto et al. 2011) or the resonance of the conduit (Watson et al. 2019). Similarly, the power of the ISC fumarole in ~ 10 Hz or ~ 35 Hz might be the resonance frequency that relates to the topography around the source. On the other hand, the ground topography is also affect the power spectral shape significantly (Yamakawa 2022). There is a small wall behind the ISC fumarole (Fig. 2c), and it might have an influence. Further investigation is needed to understand the fumarolic infrasound generation mechanisms.

6.4. The VSA array and SI microphone

In the estimation of IWC fumarole, the SI microphone close to the source played an essential role. The SI-Array CC revealed the contribution of the IWC fumarole, though the array CC failed to identify it. From the peak of the SI-Array CC, the source regions were constrained. One might question whether the VSA array was necessary or not. Here we summarize the contribution of the array. Although the peak of the IWC fumarole in a single pair of the SI-array CC was recognizable by the stacking (Fig. S5), such a peak as small as 0.01 would be difficult to conclude as a signal without the confirmation by the array analysis using all pairs of the SI-array CC. Namely, the VSA array confirmed the very small peak of the SI-array CC as a signal. Then, the array CC helped distinguish the signal from the correlation peak made of ambient noise through the synthetic tests (Section 6.2). The identification of signals from noise is essential in monitoring. In addition, the combination of the source hyperbola obtained by the two stations and the back azimuth range obtained from the array analysis on the SI-array CC constrained the source location. From above, we conclude that the VSA array could significantly improve the monitoring network.

7. Summary

In monitoring multiple infrasound sources, the identification of each source's contribution is essential. To challenge this problem, we conducted an experiment combining a VSA microphone array with a single microphone at Kirishima Iwo-Yama, where several active fumaroles persistently emanated infrasonic signals. The experiment was designed to resolve IWC and ISC fumaroles' signals. The VSA array, which was 150 m from the ISC fumarole and 300 m from the IWC fumarole, estimated the significant contribution of the ISC. All of the lag time analysis, MUSIC algorithm, and CLEAN beamforming could identify signals from the more powerful ISC, but none resolved the contribution of the IWC fumarole. However, incorporating the SI microphone placed close to the IWC fumarole, the VSA array successfully distinguished the contributions of the two sources. With some simplifications (monopole sources and homogeneous propagation), we estimated the individual source amplitudes and spectra. This study provides a tool to observe weak multiple infrasonic sources, which will be useful in volcano monitoring.

Declarations

Availability of data and materials

The data sets used and/or analyzed during the current study are available from the corresponding author on reasonable request.

Competing interests

The authors declare that they have no competing interests.

Funding

This study was funded by a Japan Society for the Promotion of Science Research Fellowship Grant-in-Aid (JSPS KAKENHI Grant Number JP19J13999), the Joint Usage of the Earthquake Research Institute, the University of Tokyo (2019B01), and the Ministry of Education, Culture, Sports, Science and Technology (MEXT) of Japan, under its Earthquake and Volcano Hazards Observation and Research Program.

Authors' contributions

KY developed the methods, made the analyses, and drafted the manuscript, supported by MI. KY, MI, DM, and TM conducted the field experiment, and HT and RW developed the MEMS infrasound sensors. IS led the project developing the MEMS infrasound sensor. All authors read and approved the final manuscript.

Acknowledgements

We thank S. Watada for constructive comment that improved our manuscript significantly. The field observation was conducted with the help of Y. Tajima, S. Aniya, and Y. Tang.

References

1. Chouet B, Saccorotti G, Martini M, Dawson P, De Luca G, Milana G, Scarpa R (1997) Source and path effects in the wave fields of tremor and explosions at Stromboli Volcano, Italy. *J Geophys Research: Solid Earth* 102(B7):15129–15150. doi:10.1029/97JB00953
2. Fee D, Garces M, Orr T, Poland M (2011) Infrasound from the 2007 fissure eruptions of Kīlauea Volcano, Hawai'i. *Geophys Res Lett* 38(6). doi:10.1029/2010GL046422
3. Fee D, Garcés M, Patrick M, Chouet B, Dawson P, Swanson D (2010) Infrasonic harmonic tremor and degassing bursts from Halema'uma'u Crater, Kilauea Volcano, Hawaii. *J Geophys Research: Solid Earth* 115(B11). doi:10.1029/2010JB007642
4. Fischer TP (2008) Fluxes of volatiles (H₂O, CO₂, N₂, Cl, F) from arc volcanoes. *Geochem J* 42(1):21–38. doi:10.2343/geochemj.42.21
5. Goto A, Johnson JB (2011) Monotonic infrasound and helmholtz resonance at Volcan Villarrica (Chile). *Geophys Res Lett* 38(6). doi:10.1029/2011GL046858
6. Ikeda W, Ichihara M, Honda R, Aoyama H, Takahashi H, Yoshimoto M, Sakai S (2021) Experiment of Infrasound Monitoring for Snow Avalanche at My. Fuji, Seppyō. (in press)
7. Johnson JB, Palma JL (2015) Lahar infrasound associated with Volcán Villarrica's 3 March 2015 eruption. *Geophys Res Lett* 42(15):6324–6331. doi:10.1002/2015GL065024
8. Marchetti E, Ripepe M, Ulivieri G, Caffo S, Privitera E (2009) Infrasonic evidences for branched conduit dynamics at Mt. Etna volcano, Italy. *Geophys Res Lett* 36(19). doi:10.1029/2009GL040070
9. McKee K, Fee D, Yokoo A, Matoza RS, Kim K (2017) Analysis of gas jetting and fumarole acoustics at Aso Volcano, Japan. *J Volcanol Geoth Res* 340:16–29. doi:10.1016/j.jvolgeores.2017.03.029
10. Minh-Dung N, Takahashi H, Uchiyama T, Matsumoto K, Shimoyama I (2013) A barometric pressure sensor based on the air-gap scale effect in a cantilever. *Appl Phys Lett* 103(14):143505. doi:10.1063/1.4824027
11. Muramatsu D, Matsushima T, Ichihara M (2021) Reconstructing surface eruptive sequence of 2018 small phreatic eruption of Iwo-yama volcano, Kirishima Volcanic Complex, Japan, by infrasound cross-correlation analysis. *Earth Planets and Space* 73(1):1–10. doi:10.1186/s40623-020-01344-6
12. Ortiz HD, Matoza RS, Johnson JB, Hernandez S, Anzieta JC, Ruiz MC (2021) Autocorrelation infrasound interferometry. *J Geophys Research: Solid Earth* 126(4) e2020JB020513. doi:10.1029/2020JB020513
13. Ripepe M, Marchetti E (2002) Array tracking of infrasonic sources at Stromboli volcano. *Geophys Res Lett* 29(22):33–31. doi:10.1029/2002GL015452
14. Ripepe M, Marchetti E, Bonadonna C, Harris AJ, Pioli L, Ulivieri G (2010) Monochromatic infrasonic tremor driven by persistent degassing and convection at Villarrica Volcano, Chile. *Geophys Res Lett* 37(15). doi:10.1029/2010GL043516
15. Salvatore V, Silleni A, Corneli D, Taddeucci J, Palladino DM, Sottili G, Bernini D, Andronico D, Cristaldi A (2018) Parameterizing multi-vent activity at Stromboli Volcano (Aeolian Islands, Italy). *Bull Volcanol* 80(7):1–17. doi: 10.1007/s00445-018-1239-8

16. Shapiro NM, Campillo M (2004) Emergence of broadband Rayleigh waves from correlations of the ambient seismic noise. *Geophys Res Lett* 31(7). doi:10.1029/2004GL019491
17. Shields DF (2005) Low-frequency wind noise correlation in microphone arrays. *J Acoust Soc Am* 117(6):3489–3496. doi:10.1121/1.1879252
18. Tajima Y, Nakada S, Maeno F, Huruzono T, Takahashi M, Inamura A, Matsushima T, Nagai M, Funasaki J (2020) Shallow magmatic hydrothermal eruption in April 2018 on Ebinokogen Ioyama volcano in Kirishima volcano group. *Kyushu Japan Geosciences* 10(5):183. doi:10.3390/geosciences10050183
19. Takahashi H, Suzuki A, Iwase E, Matsumoto K, Shimoyama I (2012) MEMS microphone with a micro Helmholtz resonator. *J Micromech Microeng* 22:085019
20. Tam C, Viswanathan K, Ahuja KK, Panda J (2008) The sources of jet noise: experimental evidence. *J Fluid Mech* 615:253–292. doi:10.1017/S0022112008003704
21. Wada R, Takahashi H (2020) Time response characteristics of a highly sensitive barometric pressure change sensor based on MEMS piezoresistive cantilevers. *Jpn J Appl Phys* 59(7):070906
22. Wallace PJ (2005) Volatiles in subduction zone magmas: concentrations and fluxes based on melt inclusion and volcanic gas data. *J volcanology Geotherm Res* 140(1–3):217–240. doi:10.1016/j.jvolgeores.2004.07.023
23. Woulff G, McGetchin TR (1976) Acoustic noise from volcanoes: Theory and experiment. *Geophys J Int* 45(3):601–616. doi:10.1111/j.1365-246X.1976.tb06913.x
24. Yamakawa K, Ichihara M, Ishii K, Aoyama H, Nishimura T, Ripepe M (2018) Azimuth estimations from a small aperture infrasonic array: test observations at Stromboli Volcano, Italy. *Geophys Res Lett* 45(17):8931–8938. doi:10.1029/2018GL078851
25. Yamakawa K (2022) Evaluation and practice of very-small-aperture infrasonic array for volcano monitoring. Dissertation, University of Tokyo
26. Yamakawa K, Ichihara M, Lacanna G, Sánchez C, Ripepe M (2022) Very-small-aperture 3-D infrasonic array for volcanic jet observation at Stromboli Volcano. *Geophys J Int* 229(1):459–471. doi:10.1093/gji/ggab487
27. Yokoo A, Suzuki Y, Iguchi M (2014) Dual infrasound sources from a vulcanian eruption of Sakurajima volcano inferred from cross-array observation. *Seismol Res Lett* 85(6):1212–1222. doi:10.1785/0220140047
28. Yokoo A, Ishii K, Ohkura T, Kim K (2019) Monochromatic infrasound waves observed during the 2014–2015 eruption of Aso volcano, Japan. *Earth Planets and Space* 71(1):1–14. doi:10.1186/s40623-019-0993-y
29. Yokoo A, Ishii K, Ohkura T, Kim K (2019) Monochromatic infrasound waves observed during the 2014–2015 eruption of Aso volcano, Japan. *Earth, Planets and Space*, 71(1), 1–14. doi:10.1186/s40623-019-0993-y

Tables

Table 1. Summary of the infrasound sources

	ISC fumarole	IWC fumarole	noise
Distance from the array	150 m	300 m	-
Distance from the SI microphone	450 m	15 m	-
Peak value of the array CC	0.80	-	-
Peak value of the SI-array CC	0.13	0.01	-
Monopole source amplitude (at 1 m)	3 Pa	0.2 Pa	-
RMS Amplitude at the array	0.0200 Pa	0.0007 Pa	0.0223 Pa
RMS Amplitude at the SI microphone	0.0067 Pa	0.0140 Pa	0.0257 Pa
Power fractions at the array	44.4 %	0.1 %	55.5 %
Power fractions at the SI microphone	5.0 %	21.8 %	73.2 %

Table 2. Test parameters and the correlation peak values

The other amplitudes in Equation 5 are fixed as $A_{noise}^n = 0$ ($n = A1, A2, A3$), and $A_k = 1$.

	ISC amplitude (θ)	IWC amplitude (θ)	Noise amplitude in SI microphone (θ)	Peak value of Array CC	Peak value of SI-array CC in +0.8 sec	Peak value of SI-array CC in -0.8 sec
Observation	-	-	-	0.90	0.13	0.01
Test 1	0	0	0	0.12	0.02	0.03
Test 2	8	0	0	0.30	0.13	0.01
Test 3	25	0	0	0.90	0.50	0.005
Test 4	25	0	0.4	0.90	0.13	None
Test 5	25	2	0.4	0.90	0.13	0.01

Figures

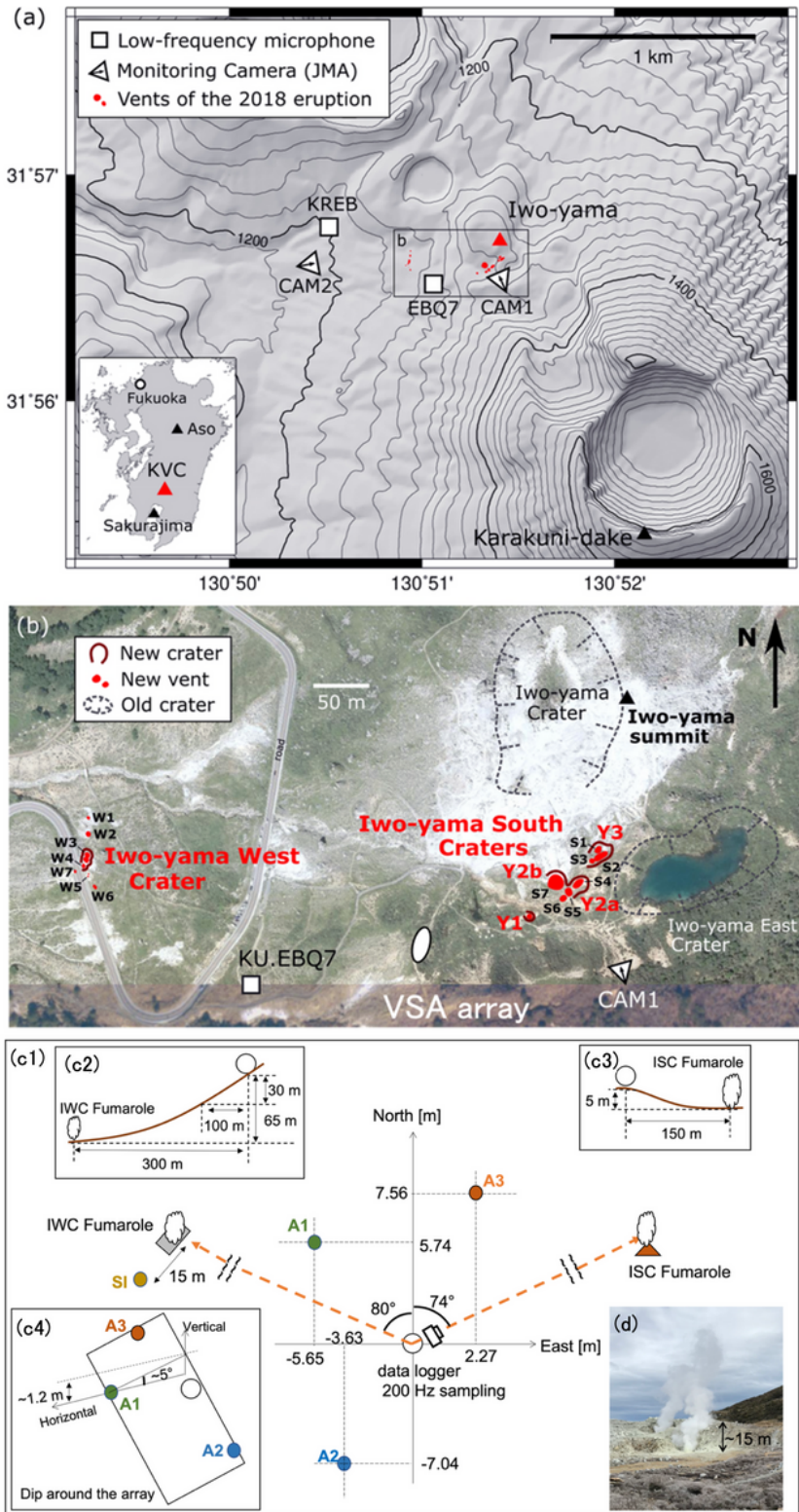


Figure 1

Kirishima Iwo-Yama and the array observation

(a) The location of Kirishima Iwo-Yama and the infrasound stations (EBQ7 and KREB) used in Muramatsu et al. (2021). (b) The craters and the location of the VSA array (white ellipse). The panels of (a) and (b) are modified from Figure 1 of Muramatsu et al. (2021). (c1) The observation geometry

consisting of the VSA array (microphones A1 A3) and the SI microphone with respect to the ISC and IWC fumaroles. (c2, c3) The topographic features between the VSA array site (white circle) and the IWC fumarole (c2) and the ISC fumarole (c3). (c4) The ground dip of the array site. (d) An image of the ISC fumarole taken from the array location (the camera symbol shown in c1).

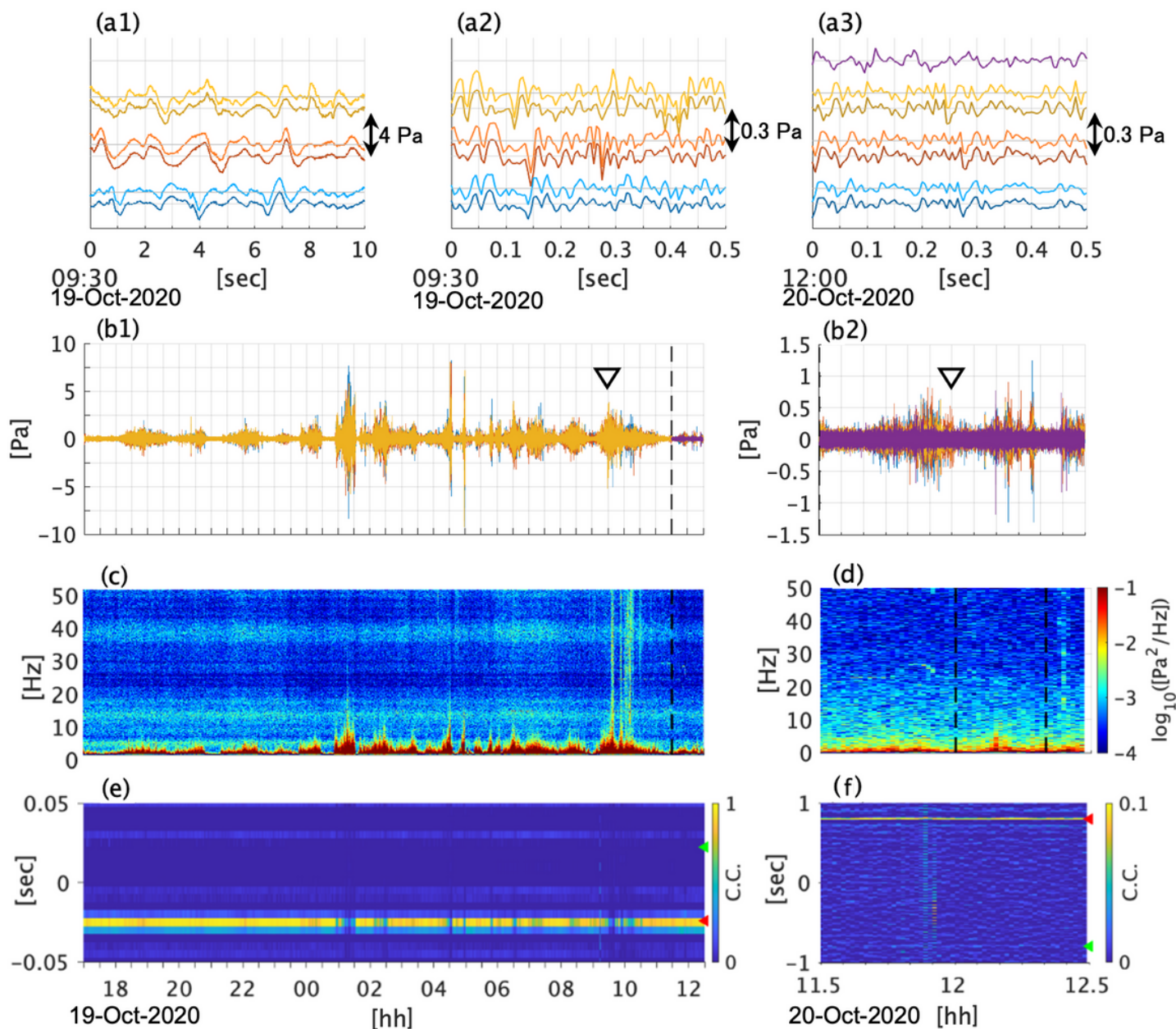


Figure 2

Waveforms, spectrograms, and correlation coefficients

(a) Examples of the observed waveforms filtered at (a1, a3) 0.3-90 Hz and (a2) 5-90 Hz. The line colors indicate the microphones (blue, A1; red, A2; yellow, A3; purple, SI). The lower darker colored lines and upper lighter colored lines in (a1-a3) indicate the waveforms recorded by ACO and MEMS microphones, respectively. (b-f) The waveforms filtered at 0.3-90 Hz (b1, b2), the spectrograms (c, d), and the cross-

correlation coefficients (e, f) during the array observation on the left (b1, c, e) and with the SI observation on the right (b2, d, f). The black dashed line in (b1) indicates the start time of (b2). The black triangles in (b1) and (b2) mark the origin times of (a1, a2) and (a3), respectively. The displayed spectrograms are of A1 (c) and SI (d), and the cross-correlation coefficients are between A1 and A3 (f) and A1 and SI (e), using the waveforms filtered from 5 to 90 Hz. The arrowheads on the right axis in (e) and (f) indicate the lag times between the microphones assuming the ISC source (red) and IWC source (green). The waveforms, spectrograms, and correlation coefficients of the other microphones are in Supporting Information S3.

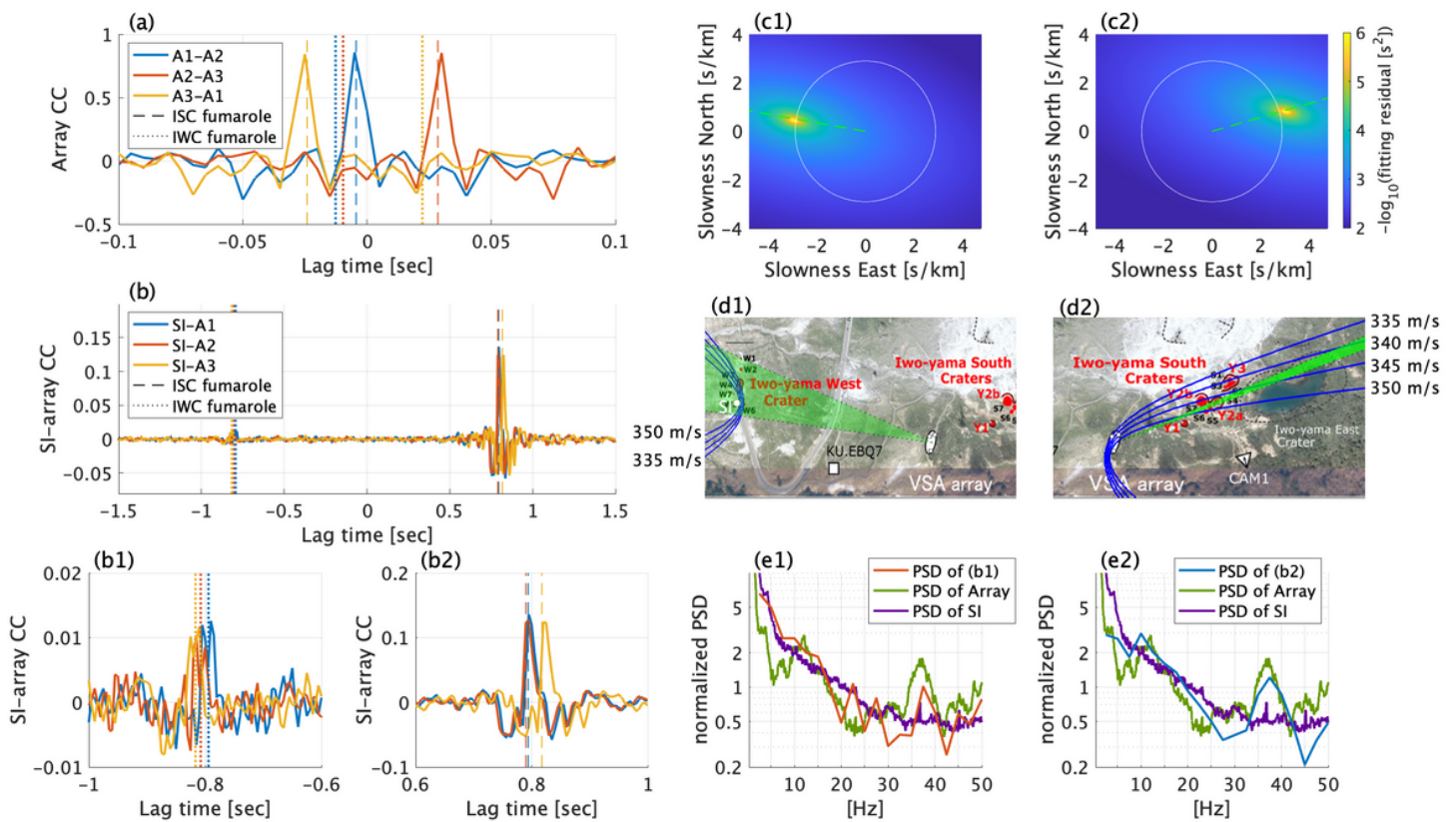


Figure 3

Correlation coefficients and the array analysis results

(a) The array CC and (b) SI-array CC in 5–90 Hz. The enlarged view of (b) around the minor peak (b1) and the prominent peak (b2). The vertical lines in these panels are the calculated infrasound propagation time differences between the microphone pairs, assuming the sources at the IWC fumarole (dotted lines in b1) and the ISC fumarole (dashed lines in b2). The lag time fitting results for the peaks in (b1) and (b2) are shown in (c1, d1) and (c2, d2), respectively. (c) The fitting residual using all pairs of SI-array CC is shown as functions of horizontal components of the slowness. The white circles indicate acoustic slowness. (d) The blue lines indicates the source hyperbola obtained from the SI–A1 lag time fitting using the assumed propagation velocities as 335, 340, 345, and 350 m/s. The two dashed lines bound the estimated back azimuth range (2 STD) obtained from (c). The white and red points mark the microphones' and

fumaroles' locations, respectively. (e) The normalized power spectral densities (PSDs) calculated using the three traces in (b1) and (b2) are shown in (e1) by the red line (e1) and in (e2) by the blue line (e2), respectively. They are compared with the PSD of the array microphones (green) and the PSD of the SI microphone (purple). For the former (the green line), the normalized PSDs of the individual array microphones are averaged.

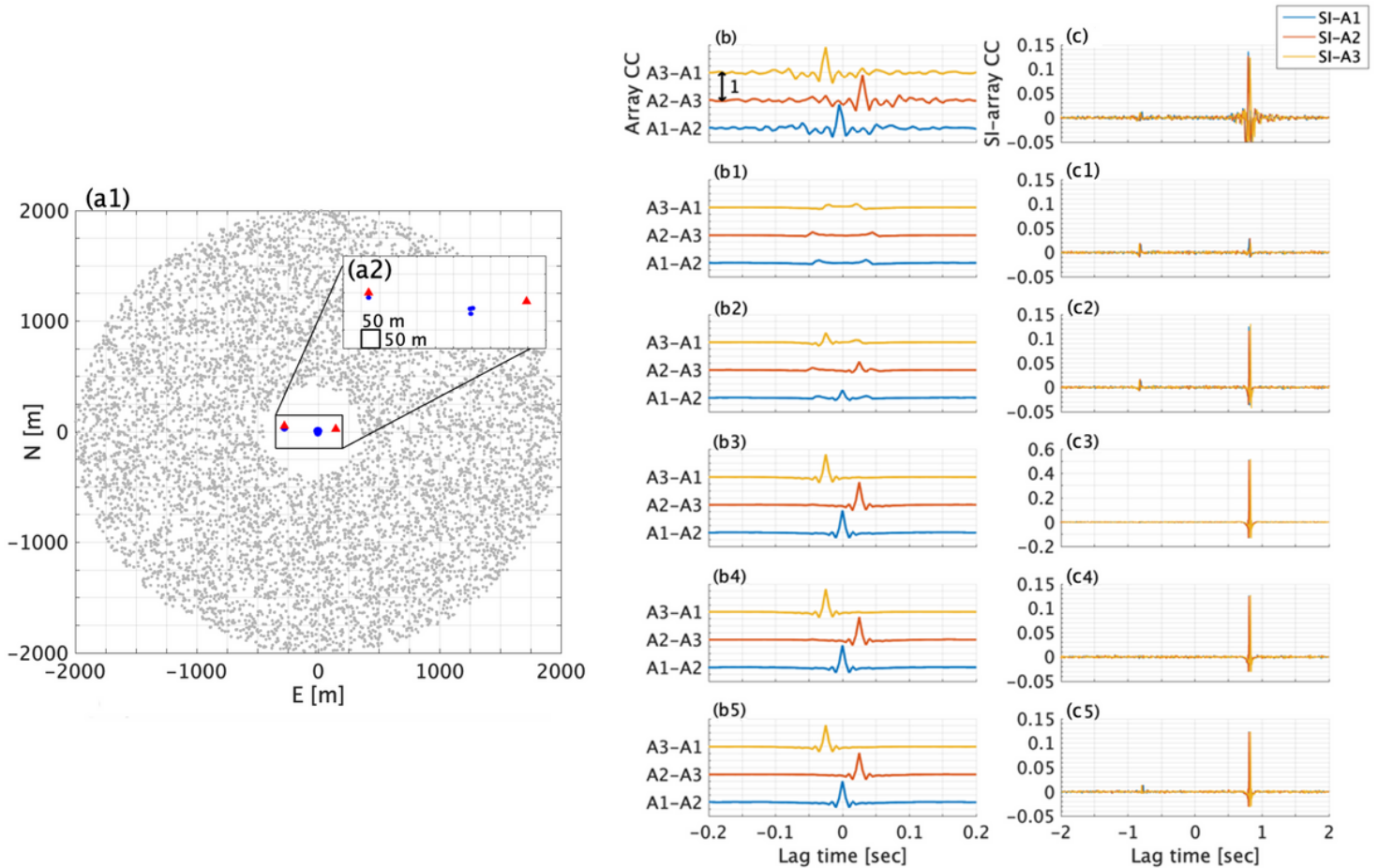


Figure 4

Ambient noise and correlation signals

(a1) The locations of the microphones (blue circles), signal sources (red triangles), and ambient noise sources (gray dots). (a2) The enlarged view of (a1). (b) Array CC and (c) SI-Array CC from the observation (b, c) and synthetic tests (b1–b5 and c1–c5 represent results of Test 1–5 to be compared with b and c, respectively). The vertical scales are identical in all panels in (b). Conditions of the synthetic tests are listed in Table 2.

Supplementary Files

This is a list of supplementary files associated with this preprint. [Click to download.](#)

- [GrphicalAbstract.png](#)
- [SupportingInformation.docx](#)